PNAS RESEARCH ARTICLE | CHEMISTRY

Gd_2O_3-mesoporous silica/gold nanoshells: A potential dual T_1/T_2 contrast agent for MRI-guided localized near-IR photothermal therapy

Yara Kadria-Vili[a,b,c], Oara Neumann[b,d], Yage Zhao[b,e], Peter Nordlander[b,d,e], Gary V. Martinez[c], James A. Bankson[c], and Naomi J. Halas[a,b,d,e,1]

Contributed by Naomi Halas; received December 31, 2021; accepted June 2, 2022; reviewed by Amit Joshi and Carly Filgueira

A promising clinical trial utilizing gold-silica core-shell nanostructures coated with polyethylene glycol (PEG) has been reported for near-infrared (NIR) photothermal therapy (PTT) of prostate cancer. The next critical step for PTT is the visualization of therapeutically relevant nanoshell (NS) concentrations at the tumor site. Here we report the synthesis of PEGylated Gd_2O_3-mesoporous silica/gold core/shell NSs (Gd_2O_3-MS NSs) with NIR photothermal properties that also supply sufficient MRI contrast to be visualized at therapeutic doses ($\geq 10^8$ NSs per milliliter). The nanoparticles have r_1 relaxivities more than three times larger than those of conventional T_1 contrast agents, requiring less concentration of Gd^{3+} to observe an equivalent signal enhancement in T_1-weighted MR images. Furthermore, Gd_2O_3-MS NS nanoparticles have r_2 relaxivities comparable to those of existing T_2 contrast agents, observed in agarose phantoms. This highly unusual combination of simultaneous T_1 and T_2 contrast allows for MRI enhancement through different approaches. As a rudimentary example, we demonstrate T_1/T_2 ratio MR images with sixfold contrast signal enhancement relative to its T_1 MRI and induced temperature increases of 20 to 55 °C under clinical illumination conditions. These nanoparticles facilitate MRI-guided PTT while providing real-time temperature feedback through thermal MRI mapping.

gadolinium oxide | gold nanoshells | MRI contrast | photothermal | mesoporous silica

Significance

Photothermal cancer therapy, based on gold nanoshells and near-infrared irradiation, has been demonstrated in a successful clinical trial for localized prostate cancer, resulting in little or no side effects for the patient. The next step in the development of this ultralocalized cancer therapy is to combine the photothermal response of the gold nanoparticles with enhanced contrast in magnetic resonance imaging, enabling a "see and treat" capability for clinicians that will facilitate the optimization of nanoparticle dosing and irradiation times. Here we report a near-infrared photothermally responsive nanoparticle with an outstanding and highly unusual MRI contrast agent with both T_1 and T_2 contrast, allowing for enhanced MR imaging capabilities.

Nanoparticle-mediated photothermal therapy (PTT) has attracted extensive research attention for the ultralocalized treatment of solid tumors. In a clinical trial using nontargeted silica/gold core/shell nanoshells (NSs) functionalized with polyethylene glycol (PEG), remarkably high rates of tumor ablation were observed for early-stage prostate cancer, with over a 90% success rate at 1 y posttreatment. Even more remarkably, the rate of morbidity posttreatment was negligible, with patients reporting no increase in incontinence and the preservation of sexual function (1).

To date, a variety of nanoparticles (NPs) have been developed for PTT, including metallic NPs, carbon-based NPs, and organic/inorganic nanohybrid NPs (2). Gold NSs under near-infrared (NIR) light [at wavelengths where tissue is highly transparent (3, 4) and ∼3 cm penetration depth is possible] (5) have opened an additional avenue to photothermally treat solid tumors. NIR illumination at the NS plasmon resonance induces collective oscillations of the NS conduction band electrons, causing an increase in local temperature that can initiate various cell death pathways (6). While the initial prostate cancer data are promising (1), PTT outcomes and treatment protocols could be further improved by enhancing NS uptake, retention, and visualization of their intratumoral distribution. Furthermore, real-time temperature evaluation of the ablated tumor and the surrounding healthy tissue during the PTT procedure is crucial to precisely control the tissue's thermal conditions and prevent excessive or partial treatment. Various imaging modalities, such as MRI (7, 8), ultrasound imaging (9), and photoacoustic imaging (10), have been applied to monitor temperature noninvasively during PTT. While temperature-dependent optical properties of tissues limit photoacoustic (11, 12) and ultrasound signals (13, 14), MRI can assist in photothermal treatment by providing thermal, anatomical, and functional images (1, 8, 15, 16). Thus, MRI is a promising optical tool in medical diagnosis and treatment. Furthermore, thermal MRI mapping has been shown to correlate thermal damage with the extent of thermal necrosis (17, 18) and enable real-time temperature evaluation during PTT (8, 19–21). Temperatures above 49 °C will initiate the necrosis cell death pathway that induces inflammation and secondary tumor formation (22). A highly controlled temperature increase within the range of 46 to 49 °C is reported to be ideal for tumor elimination by apoptosis (23) and necroptosis cell death pathways (24–26). Nanoparticle (NP)-assisted PTT that triggers apoptosis or necroptosis has been targeted by tuning experimental parameters such as

Author affiliations: [a]Department of Chemistry, Rice University, Houston, TX 77005; [b]Laboratory for Nanophotonics, Rice University, Houston, TX 77005; [c]Department of Imaging Physics, The University of Texas M. D. Anderson Cancer Center, Houston, TX 77030; [d]Department of Electrical and Computer Engineering, Rice University, Houston, TX 77005; and [e]Department of Physics and Astronomy, Rice University, Houston, TX 77005

Author contributions: Y.K.-V., J.A.B., and N.J.H. designed research; Y.K.-V., O.N., and G.V.M. performed research; O.N., Y.Z., and P.N. contributed new reagents/analytic tools; Y.K.-V., Y.Z., P.J.N., and G.V.M. analyzed data; and Y.K.-V., P.N., J.A.B., and N.J.H. wrote the paper.

Reviewers: C.F., Houston Methodist; and A.J., Medical College of Wisconsin.

Competing interest statement: A patent is being filed on the nanoparticle whose synthesis and properties we report in this manuscript.

[1]To whom correspondence may be addressed. Email: halas@rice.edu.

This article contains supporting information online at http://www.pnas.org/lookup/suppl/doi:10.1073/pnas.2123527119/-/DCSupplemental.

Published July 11, 2022.

laser power, exposure time, and the NPs-based PTT agent concentration (27–29). PTT has also been reported to increase the sensitivity of drug-resistant cancer cells to secondary treatments, such as chemotherapy, by enhancing the permeability of tumor cell membranes and tumor vasculatures (30–33).

This work describes a "see and treat" strategy that combines MR imaging with NIR PTT monitored by thermal MRI mapping in 0.48% agarose phantoms. We report the synthesis of a Gd_2O_3-mesoporous silica core with a gold shell nanostructure (Gd_2O_3-MS NS) with unique dual T_1 and T_2 MRI contrast properties. The structure has a strong optical signal in the NIR window, where oxygenated/deoxygenated blood and water have minimum absorption. The MRI and the NIR-photothermal capabilities of Gd_2O_3-MS NSs make the structure ideal for MRI-guided PTT. Gd_2O_3-MS NSs at concentrations equivalent to current therapeutic concentrations (1.15 to 33.12 μg gold per gram of tumor tissue corresponding to 0.78 to 22.6 × 10^8 NSs per milliliter) (1) in agarose phantoms were found to provide sufficient contrast in MRI, to enable localized photothermal heating under NIR illumination, and to facilitate real-time temperature feedback through thermal MRI mapping. Under identical illumination conditions to those used in clinical practice (3-min illumination of 810 nm coupled with 10-mm diffuser tip at 4 W), a concentration range of (1.1 to 8.4) × 10^9 Gd_2O_3-MS NSs per milliliter was sufficient to cause a temperature change of 20 to 55 °C in agarose phantoms. Furthermore, their dual T_1 and T_2 MRI properties are shown to enhance MRI visualization in T_1-weighted (T_1w) MRI and T_2-weighted (T_2w) MRI. To demonstrate that additional contrast approaches may be possible, we provide a simple example, showing how their MRI contrast signal can be further enhanced by processing the ratio of T_1w/T_2w signal intensities (34–37). Our results suggest that Gd_2O_3-MS NSs can boost contrast in the processed MR image of the T_1w/T_2w signal intensity ratio, facilitate real-time temperature feedback under thermal MRI mapping, and enhance PTT efficacy. In future in vivo studies, these particles will be visualized with MRI, providing more information for their biodistribution within a solid tumor, which is critical for effective treatment planning, targeting areas where a high concentration of particles is located. Furthermore, Gd_2O_3-MS NSs' capability for imaging and focal thermal therapy of solid tumors will need to be validated and their dosage (number of NSs per gram of tissue) and route of administration will need to be investigated for each type of cancer.

Results

Synthesis of Gadolinium Oxide Mesoporous Silica Gold Nanoshells. A representation of the gadolinium oxide mesoporous silica gold nanoshells (Gd_2O_3-MS NSs) synthesis with corresponding transmission electron microscopy (TEM) images at each stage of the process is shown in Fig. 1*A* and *B*. Mesoporous silica (MS) cores were synthesized according to the Stöber method with minor modifications from the literature (38). Fig. 1*B*, *i* and *ii* shows TEM images before and after a hexadecyltrimethylammonium chloride (CTAC) template was sufficiently decomposed through baking at 500 °C, generating pores within the silica core. Nitrogen adsorption–desorption isotherm measurements and Brunauer–Emmett–Teller (BET) data indicate that the MS cores have a surface area of 907 m^2/g with an average diameter pore size of 2.5 ± 0.5 nm (*SI Appendix*, Fig. S1). Ultrasmall Gd_2O_3 nanoparticles were fabricated using an adapted protocol (38–40) with an average hydrodynamic diameter of 1.5 ± 0.1 nm (mean ± SE), determined by dynamic light scattering measurements of three batches of Gd_2O_3 nanoparticles in a diethylene glycol suspension. The Gd_2O_3 nanoparticles were loaded into the pores of the MS cores through vigorous sonication (Fig. 1*B*, *iii*). TEM measurements revealed an average diameter distribution of 95 ± 1.5 nm (mean ± SE) for the Gd_2O_3-MS cores (*SI Appendix*, Fig. S2). The Gd_2O_3-MS surface was functionalized with (3-aminopropyl)-triethoxysilane (APTES) molecules, which enabled the attachment of ∼2 to 3 nm of colloidal gold onto the Gd_2O_3-MS surface (Fig. 1*B*, *iv*). Following this step, an electroless plating process reduced more gold onto the NP surface, forming a continuous gold shell. The Gd_2O_3-MS NSs were then functionalized with a monolayer of 2 kDa methoxy-polyethylene glycol thiol (2k-PEG) to improve NS stability, facilitate the bypassing of the immune system, and increase circulation time in anticipated future in vivo studies (Fig. 1*B*, *v*). The presence of the Gd_2O_3 contrast agent (CA) within the 2k-PEGylated Gd_2O_3-MS NSs was confirmed by the scanning TEM high-angle annular dark-field (STEM-HAADF) image and energy-dispersive X-ray element mapping (Fig. 1*C*). The concentration of Gd^{3+} per NS was determined (*SI Appendix*, Eq. **S1**) to be (3.3 ± 0.1) × 10^6 Gd^{3+} per NS for 2k-PEGylated Gd_2O_3-MS NSs. Three samples of 2k-PEGylated Gd_2O_3-MS NSs were prepared with various gold shell thicknesses (22.3 ± 0.1, 27.5 ± 0.1, and 31.0 ± 0.2 nm) (mean ± SE) (Fig. 1*D*). Their extinction spectra in aqueous suspensions were measured, revealing a redshift in the plasmon resonance with an increase in gold shell thickness (≥20 nm), as predicted by Mie theory (Fig. 1*E* and *SI Appendix*, Fig. S3).

MRI Property of Gd_2O_3-MS NSs at 4.7 T. The MRI contrast of Gd_2O_3-MS NSs was determined by measuring the longitudinal magnetization recovery at various repetition times (TR) and the transverse magnetization decay at multiple echo times (TE) of water protons in the presence of numerous Gd^{3+} concentrations (Fig. 2*A* and *B*). The total water signal (S) at a known Gd^{3+} concentration (Fig. 2*A* and *B*) was fitted with Eq. 1 to determine its longitudinal (T_1) and transverse (T_2) relaxation time constants:

$$S = S_0(1 - e^{-TR/T_1})e^{-TE/T_2}, \quad [1]$$

where S_0 is a scaling factor. Increasing Gd^{3+} concentration shortens both T_1 and T_2 relaxation times of the neighboring water protons, causing an increase in signal intensity at the T_1w MRI and a decrease in signal intensity at the T_2w MRI (Fig. 2*C* and *D*, respectively). Plotting R_1 ($1/T_1$) and R_2 ($1/T_2$) relaxation rate constants as a function of Gd^{3+} concentrations for 2k-PEGylated Gd_2O_3-MS NSs with a 22.3-nm gold shell shows a linear dependence with slope values of r_1 = 15.8 ± 0.6 $mM_{Gd}^{-1}{\cdot}s^{-1}$ (5.2 × 10^7 $mM_{NS}^{-1}{\cdot}s^{-1}$) and r_2 = 120 ± 5 $mM_{Gd}^{-1}{\cdot}s^{-1}$ (4.04 × 10^8 $mM_{NS}^{-1}{\cdot}s^{-1}$) (Fig. 2*E* and *SI Appendix*, Fig. S4).

In general, T_1 contrast agents have a r_2/r_1 ratio < 5, while T_2 contrast agents have r_2/r_1 ratio > 10 (42). The 2k-PEGylated Gd_2O_3-MS NSs have an r_2/r_1 ratio of 7.6 ± 0.4, which could be considered a T_1 and a T_2 contrast agent. The r_1 and r_2 relaxivity values and their r_2/r_1 ratio for each Gd_2O_3-MS NS at various stages of the synthesis were calculated (*SI Appendix*, Fig. S5); the values were compared with those of other T_1 contrast agents (Magnevist) and T_2 contrast agents (Ferumoxide, Resovist) (41) currently in widespread clinical use (Fig. 2*F* and *G*). The r_1 (15.8 ± 0.7 $mM_{Gd}^{-1}{\cdot}s^{-1}$) relaxivity value of an aqueous suspension of 2k-(COOH) PEGylated Gd_2O_3 at 4.7 T is comparable to literature values of r_1 = 8.8 $mM_{Gd}^{-1}{\cdot}s^{-1}$ (2.2 nm at 7 T) (39) and r_1 = 14.9 $mM_{Gd}^{-1}{\cdot}s^{-1}$ (∼2 nm at 0.5 T) (43) (*SI Appendix*, Tables S1 and S2), as the changes in r_1 relaxivity values for

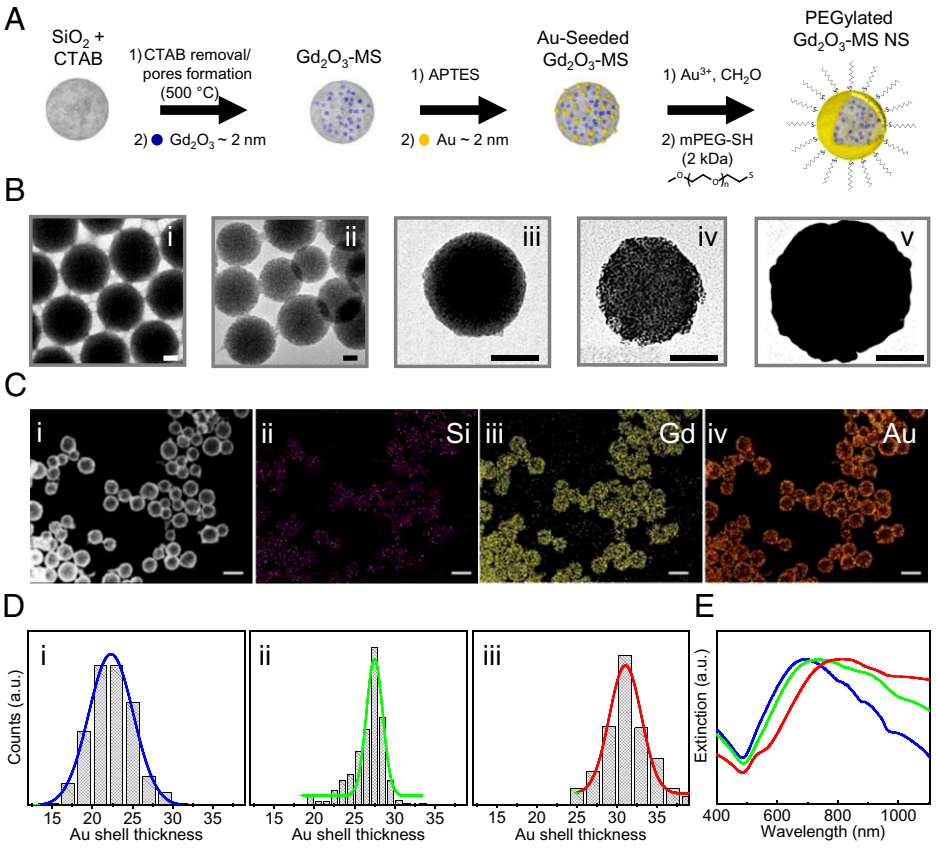

Fig. 1. Synthesis and characterization of 2k-PEGylated Gd_2O_3-MS NSs. (*A*) A schematic representation of the steps involved in synthesizing 2k-PEGylated MRI active Gd_2O_3-MS NS. A 95 ± 16-nm diameter of MS silica particles was incubated with ~2 nm Gd_2O_3 NPs and sealed with Au shell to form Gd_2O_3-MS NSs. The Gd_2O_3-MS NS nanoparticle was stabilized by adsorbing 2 kDa methoxy PEG molecules onto its surface through their thiol group. (*B*) TEM images corresponding to each step of the 2k-PEGylated Gd_2O_3-MS NS synthesis: (*i* and *ii*) cores of silica (*i*) before and (*ii*) after CTAC removal through 4 h of baking at 500 °C, (*iii*) Gd_2O_3-MS, (*iv*) Au-seeded Gd_2O_3-MS, and (*v*) 2k-PEGylated Gd_2O_3-MS NS. (Scale bar: 50 nm.) (*C*) (*i*) A high-resolution STEM image of a 2k-PEGylated Gd_2O_3-MS NS sample with STEM-HAADF imaging mode and its elemental mapping images correspond to (*ii*) Si, (*iii*) Gd, and (*iv*) Au atoms present in the sample. (Scale bar: 200 nm.) (*D*) Gold-shell thickness distributions of three samples of 2k-PEGylated Gd_2O_3-MS NSs determined by high resolution TEM image analysis. The distributions were fitted with a Gauss function utilizing OriginPro 2021b, giving an average shell thickness ± SE of (*i*) 22.3 ± 0.1 nm (305 NSs), (*ii*) 27.5 ± 0.1 nm (339 NSs), and (*iii*) 31.0 ± 0.2 nm (297 NSs). (*E*) Their corresponding extinction spectra in Milli-Q water with the same color code (blue, 22.3 nm; green, 27.5 nm; and red, 31.0 nm).

Gd-based contrast agents are small and inversely proportional to the external magnetic strength (41, 44). Embedding Gd_2O_3 nanocrystals (r_1 = 15.8 ± 0.7 $mM_{Gd}^{-1}{\cdot}s^{-1}/Gd^{3+}$; r_2 = 30.6 ± 0.3 $mM_{Gd}^{-1}{\cdot}s^{-1}/Gd^{3+}$) within Gd_2O_3-MS NSs did not affect r_1 (15.8 ± 0.6 $mM_{Gd}^{-1}{\cdot}s^{-1}/Gd^{3+}$) but enhanced r_2 by nominally a factor of 4 for Gd_2O_3-MS NSs with a gold shell thickness of 22.3 ± 0.1 nm (Fig. 2*F* and *G*). Increasing the shell thickness to 27.5 ± 0.1 nm and 31.0 ± 0.2 nm, respectively, decreased the r_1 and r_2 relaxivity values to r_1 = 8.3 ± 0.2 $mM_{Gd}^{-1}{\cdot}s^{-1}/Gd^{3+}$, r_2 = 66 ± 3 $mM_{Gd}^{-1}{\cdot}s^{-1}/Gd^{3+}$ and r_1 = 3.6 ± 0.1 $mM_{Gd}^{-1}{\cdot}s^{-1}/Gd^{3+}$, r_2 = 41 ± 3 $mM_{Gd}^{-1}{\cdot}s^{-1}/Gd^{3+}$, respectively, as predicted by Solomon–Bloembergen–Morgan (SBM) theory (*SI Appendix*, Eq. **S2**) (43, 45, 46) (Fig. 2*H*). No statistically significant changes were observed in the r_2/r_1 ratio values with the increase of the gold shell thickness from 22.3 ± 0.1 nm to 27.5 ± 0.1 nm. However, the r_2/r_1 ratio for Gd_2O_3-MS NSs with a shell thickness of 31.0 ± 0.2 nm versus thinner shell thicknesses (22.3 and 27.5 nm) has statistically significantly increased to 11.4 ± 0.9 (P value ≤ 0.001), making these particles unsuitable as a T_1 contrast agent. To evaluate these nanoparticles' MRI stability and reproducibility in time, the MRI properties for 2k-PEGylated Au-seeded Gd_2O_3-MSs and 2k-PEGylated Gd_2O_3-MS NSs were remeasured 7 wk postsynthesis. For this set of measurements, new dilutions were prepared, MRI measurements were performed, and the r_1 and r_2 relaxivity rates and their r_2/r_1 ratio were calculated (*SI Appendix*, Fig. S6). The Gd_2O_3-MS NSs with 22.3 ± 0.1 nm and 27.5 ± 0.1 nm gold shells were used for further experimentation. Both samples provided sufficient contrast enhancement and a strong NIR plasmon resonance to perform MRI-guided PTT.

The Ratio of T_1w/T_2w Signal Intensities with Gd_2O_3-MS NSs. Four NMR tubes were prepared with a band of 2k-PEGylated Gd_2O_3-MS NSs (27.5 nm gold shell) in 0.48% agarose suspension at various NS concentrations (1.1×10^9, 2.1×10^9, 4.2×10^9, and 8.4×10^9 Gd_2O_3-MS NSs per milliliter) (*SI Appendix*, Fig. S7). Their T_1 and T_2 maps were established, and their MRI properties were evaluated, giving stable and reproducible r_1 (11.8 ± 0.9 $mM_{Gd}^{-1}{\cdot}s^{-1}$) and r_2 (61 ± 11 $mM_{Gd}^{-1}{\cdot}s^{-1}$) relaxivity rates at 10 mo postsynthesis (*SI Appendix*, Fig. S8). As observed earlier, increasing 2k-PEGylated Gd_2O_3-MS NSs has improved the signal contrast (SC) in T_1w and T_2w images by enhancing the signal in T_1w MRI and suppressing that in T_2w MRI. By taking the ratio of T_1w/T_2w signal intensities, the obtained processed MRI gave a better contrast with a higher signal-to-noise ratio. For processing the MR image intensity with the T_1w/T_2w ratio, the T_1w and T_2w images with the optimum SC were applied. The optimum T_1 and T_2 SCs were established using T_1w MRI with TE = 9.9 ms and TR = 1,580 ms and T_2w MRI with TE = 250 ms and

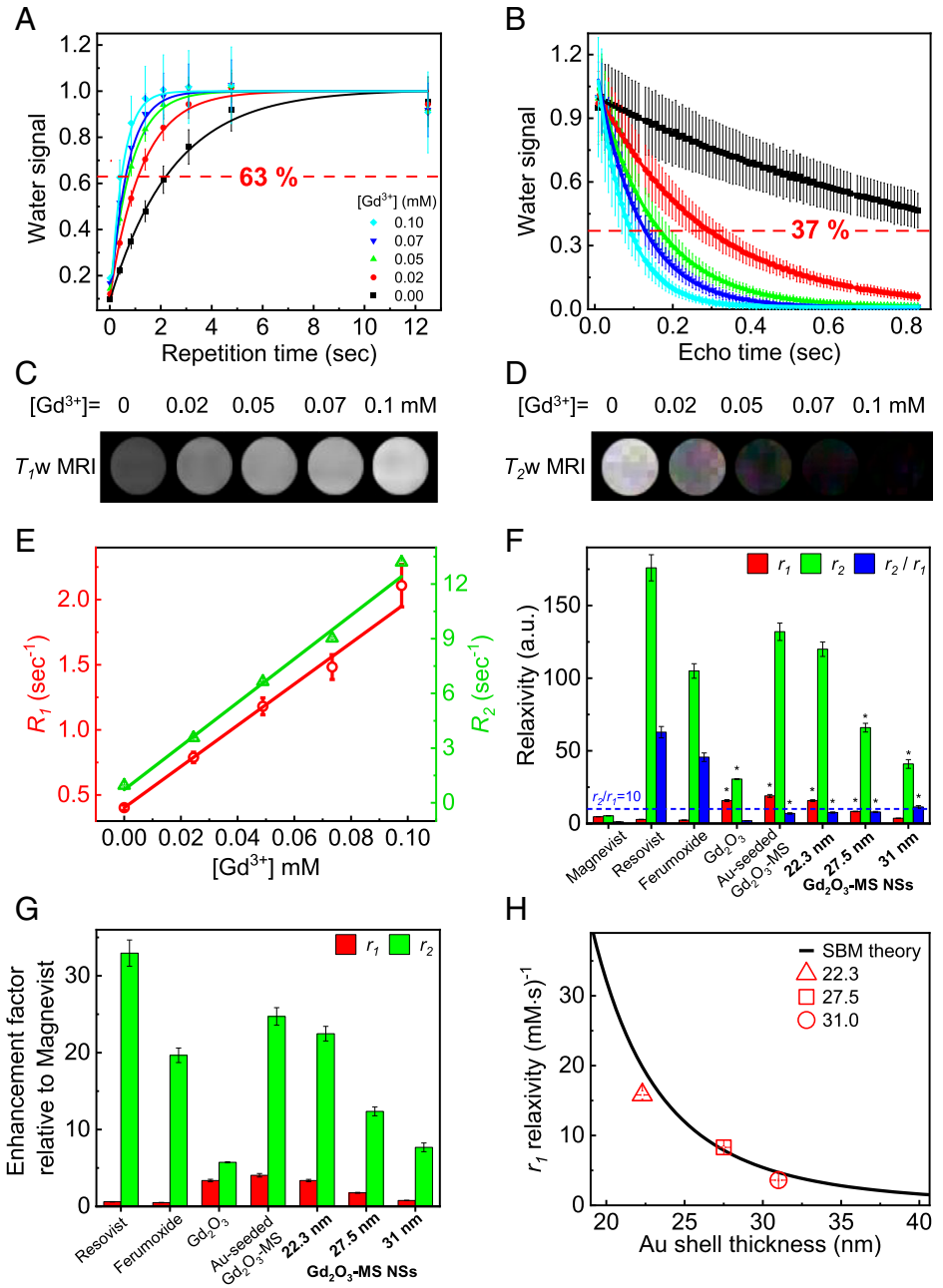

Fig. 2. MRI characterization of 2k-PEGylated Gd_2O_3-MS NSs in Milli-Q water at 4.7 T, 20 °C. (*A–D*) Longitudinal magnetization recovery (T_1), transverse magnetization decay (T_2), and their T_1w and T_2w MR images, respectively, at various gadolinium concentrations of Gd_2O_3-MS NSs with a gold shell thickness of 22.3 ± 0.1 nm. Dots are experimental data ± SD and solid lines are the fit functions using Eq. 1. The data in *A* and *B* were obtained with a RARE spin–echo sequence that loops across a range of repetition time values and MSME spin–echo scanning, respectively. T_1w MR imaging parameters: TR = 400 ms, TE = 9.9 ms, flip angle (FA) = 180°. T_2w MR imaging parameters: TR = 1,750 ms, TE = 423 ms, FA = 180°. (*E*) The inverse of T_1 (R_1, open red circles) and the inverse of T_2 (R_2, open green triangle) relaxivity rate constants at various gadolinium concentrations gave slope values of r_1 = 15.8 ± 0.6 $mM_{Gd}^{-1}{\cdot}s^{-1}$ and r_2 = 120 ± 5 $mM_{Gd}^{-1}{\cdot}s^{-1}$ (mean ± SE), respectively, for Gd_2O_3-MS NSs (22.3 ± 0.1 nm Au). (*F*) r_1 (red) and r_2 (green) relaxivity rates, and their r_2/r_1 ratio (blue) for an aqueous suspension of 2k-PEGylated Gd_2O_3 as synthesized (15.8 ± 0.7 $mM_{Gd}^{-1}{\cdot}s^{-1}$, 30.6 ± 0.3 $mM_{Gd}^{-1}{\cdot}s^{-1}$, 1.94 ± 0.09), Au-seeded Gd_2O_3-MS (19 ± 1 $mM_{Gd}^{-1}{\cdot}s^{-1}$, 132 ± 6 $mM_{Gd}^{-1}{\cdot}s^{-1}$, 6.9 ± 0.5), and Gd_2O_3-MS NSs with gold shell thicknesses of 22.3 ± 0.1 nm (15.8 ± 0.6 $mM_{Gd}^{-1}{\cdot}s^{-1}$, 120 ± 5 $mM_{Gd}^{-1}{\cdot}s^{-1}$, 7.6 ± 0.4), 27.5 ± 0.1 nm (8.3 ± 0.2 $mM_{Gd}^{-1}{\cdot}s^{-1}$, 66 ± 3 $mM_{Gd}^{-1}{\cdot}s^{-1}$, 8.0 ± 0.4), and 31.0 ± 0.2 nm (3.6 ± 0.1 $mM_{Gd}^{-1}{\cdot}s^{-1}$, 41 ± 3 $mM_{Gd}^{-1}{\cdot}s^{-1}$, 11.4 ± 0.9) in comparison with a T_1 contrast agent (Magnevist: 4.7 ± 0.1 $mM_{Gd}^{-1}{\cdot}s^{-1}$, 5.34 ± 0.04 $mM_{Gd}^{-1}{\cdot}s^{-1}$, 1.14 ± 0.03) and T_2 contrast agents (Resovist, 2.8 ± 0.1 $mM_{Gd}^{-1}{\cdot}s^{-1}$, 176 ± 9 $mM_{Gd}^{-1}{\cdot}s^{-1}$, 63 ± 4; Ferumoxide, 2.3 ± 0.1 $mM_{Gd}^{-1}{\cdot}s^{-1}$, 105 ± 5 $mM_{Gd}^{-1}{\cdot}s^{-1}$, 46 ± 3). The blue dashed line is r_2/r_1 ratio = 10. Results show that Gd_2O_3, Au-seeded Gd_2O_3, and Gd_2O_3-MS NSs (Au shell thickness: 22.3 ± 0.1 nm and 27.5 ± 0.1 nm) have statistically higher r_1 relaxivity values than Magnevist (*$P < 0.001$ vs. Magnevist by ANOVA with Tukey's honestly significant difference post hoc test). (*G*) Enhancement factors r_1 (red) and r_2 (green) relative to Magnevist. Relaxivity values Resovist and Ferumoxide were taken from reference (41). (*H*) r_1 relaxivity values versus gold shell thickness. The SBM theoretical data (black solid line) with 3.3×10^6 Gd^{3+} per Gd_2O_3-MS NS is in good agreement with the experimental data (red symbols), r^2 = 0.74. Error bars are represented in *E–H* as ± SE.

TR = 3,857 ms, respectively (Fig. 3*A* and *B*). This was determined by subtracting the fitted signals for each of the 2k-PEGylated Gd_2O_3-MS NS dilutions from that for the reference (water) over a range of TE and TR values (*SI Appendix*, Fig. S8). The T_2w image with a shorter echo time (e.g., TE = 83 ms) was also considered because it is more likely to be used in the clinic. Increasing the TE from 83 to 250 ms and 425 ms increased the contrast and suppressed the signal intensity in T_2w MRI with increasing 2k-PEGylated Gd_2O_3-MS NS concentrations (Fig. 3*C* and *D*). With (1.1 to 8.4) × 10^9 2k-PEGylated Gd_2O_3-MS NSs per milliliter (0.006 to 0.046 mM estimated Gd^{3+}), the average signal intensity of water in T_1w MRI was increased by

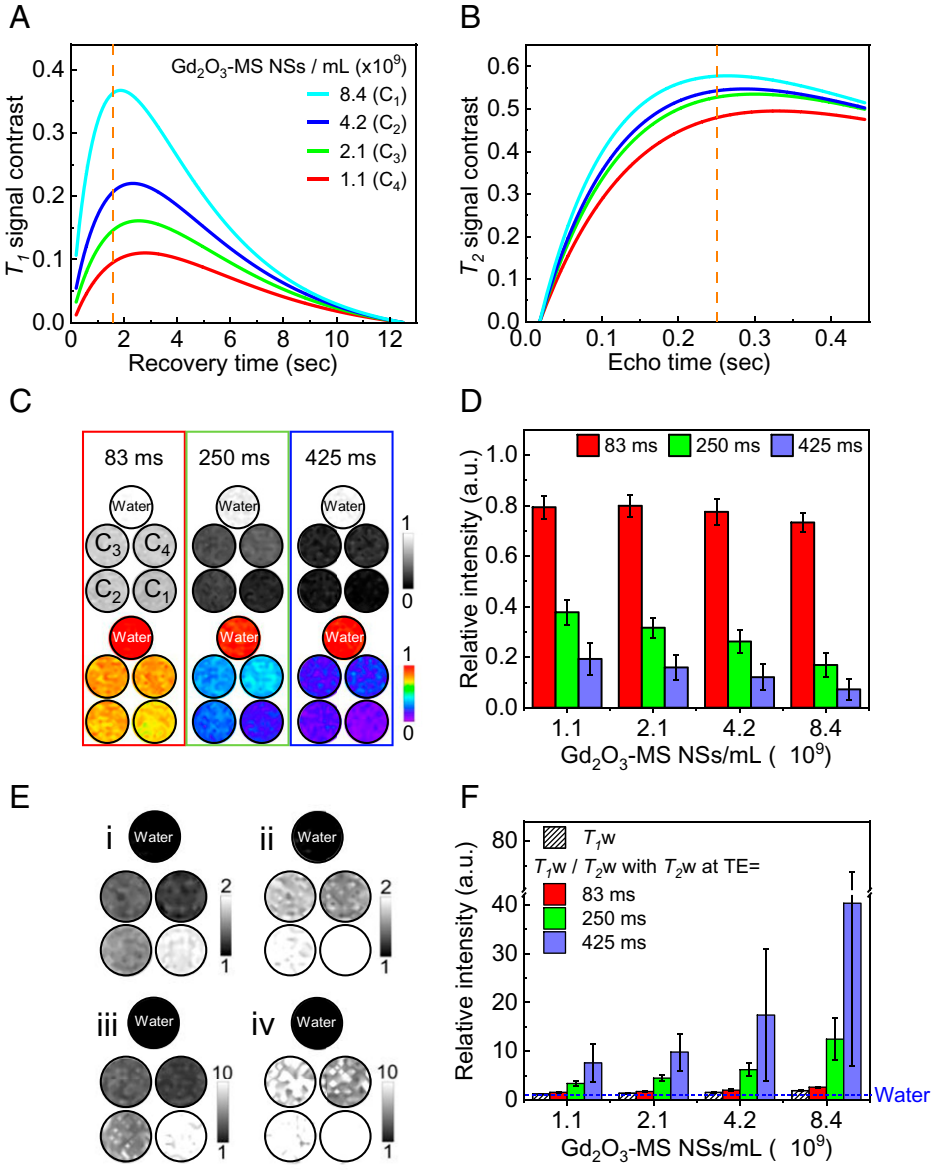

Fig. 3. MR imaging processing of T_1w/T_2w intensity ratio with 2k-PEGylated Gd_2O_3-MS NSs (27.5 ± 0.1 nm gold shell) in 0.48% agarose phantoms performed under 4.7 T magnetic strength. (*A* and *B*) T_1 and T_2 signal contrast for agarose phantoms consisting of 1.1 × 10^9 (C_4, red), 2.1 × 10^9 (C_3, green), 4.2 × 10^9 (C_2, blue), and 8.4 × 10^9 (C_1, cyan) Gd_2O_3-MS NSs per milliliter. The profiles were obtained by subtracting the fitted longitudinal recovery and the fitted transverse decay, respectively, for each Gd_2O_3-MS NS dilution from Milli-Q water. Orange dashed lines indicate the repetition time (TR = 1,580 ms) and the echo time (TE = 250 ms) at which the optimum T_1 and T_2 signal contrast, respectively, can be achieved. (*C* and *D*) T_2w MR images (*Upper*, gray scale; *Lower*, color scale) and their corresponding signal intensities at echo times = 83 ms (red), 250 ms (green), and 425 ms (purple) for various concentrations of 2k-PEGylated Gd_2O_3-MS NSs relative to that for Milli-Q water. (*E*) MR images acquired with TE = 9.9 ms and TR = 1,580 ms (*i*) and images of the processed T_1w/T_2w intensity ratio with T_2w MRI at TR = 3,857 ms and TE = 83 ms (*ii*), 250 ms (*iii*), and 425 ms (*iv*) for 2k-PEGylated Gd_2O_3-MS NSs at various concentrations. (*F*) Their corresponding MRI signal intensities relative to water signal (= 1). The values and the error bars are the mean ± SD. The data for T_1w MR images and T_2w MR images were obtained utilizing RARE sequence (TR = 1,580 ms, TE = 9.9 ms, flip angle = 180°) and MSME (TR = 3,857 ms; TE = 83 ms, 250 ms, or 425 ms; and flip angle = 180°), respectively.

1.54 ± 0.04-fold (mean ± SD) (Fig. 3*F*) while in T_2w MRI was reduced to ∼80, ∼38, and ∼19% at TE = 80, 250, and 425 ms, respectively (Fig. 3*D*). Nevertheless, processing the T_1w/T_2w intensity ratio enhanced the average contrast to water by 2.01 ± 0.07-, 7 ± 1-, and 19 ± 9-fold (mean ± SD) with T_2w MR images at TR = 3,857 ms and TE = 80, 250, and 425 ms, respectively (Fig. 3*E* and *F*).

High SD values for the processed T_1w/T_2w ratio were evident at TE = 425 ms due to T_2w images' increased sensitivity to noise at longer echo times, giving statistically significant differences at the 0.5 level. For the four concentrations of NSs ranging from 1.1 × 10^9 to 8.4 × 10^9 Gd_2O_3-MS NSs per milliliter (n = 4), a relative average intensity (RAI) of 19 ± 25 (mean ± SD) was obtained with T_1w/T_2w intensity ratio processing with T_2w MRI at TR = 3,857 ms and TE = 425 ms. The enhancement in the RAI was statistically different from that obtained with T_1w/T_2w intensity ratio processing with T_2w MRI at TR = 3,857 ms and TE = 83 ms (RAI = 2.0 ± 0.3, P value = 0.2715) or with T_1w alone (RAI = 1.5 ± 0.2, P value = 0.2515) utilizing one-way ANOVA with Tukey's honestly significant difference post hoc test.

Gd_2O_3-MS NSs-Mediated MRI-Guided PTT with Real-Time MR Temperature-Sensitive Imaging Feedback. In MRI, the shift in the proton resonance frequency of water is temperature sensitive. Slight changes in the resonance frequency caused by

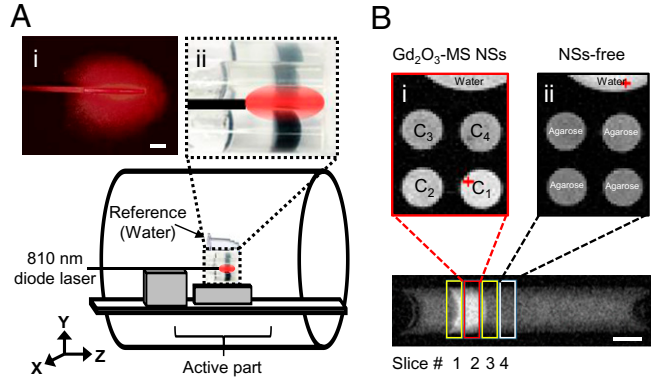

Fig. 4. Experimental setup for 2k-PEGylated Gd_2O_3-MS NSs-assisted MRI-guided PTT. (*A, Lower*) A schematic representation of the MRI-guided photothermal illumination setup showing the sample placed in the active field of the 72-mm ID MRI coil and water sample as the reference. The samples were illuminated with a CW-GaAlAs Laser diode (810 ± 20 nm) coupled with Visualase laser diffusing fiber. (*A, Upper*) Set of snapshot images of (*i*) a diffusing tip illumination profile of the 635 to 655 nm aiming beam illumination and (*ii*) a superimposed image of the sample with a cartoon image of the diffuser tip illustrating the way it was set up during the thermal MRI measurements. (*B, Lower*) Coronal T_1w MR image obtained before PTT with a fast-spoiled gradient-echo (fSPGR) sequence, TR = 275 ms, TE = 5.1 ms, number of averages = 2, FA = 90°, FOV = 35 mm, and matrix size = 256 × 256. (*B, Upper*) Axial T_1w MR images at the (*i*) 2k-PEGylated Gd_2O_3-MS NSs location (slice 2), consisting of 1.1 × 10^9 (C_4), 2.1 × 10^9 (C_3), 4.2 × 10^9 (C_2), and 8.4 × 10^9 (C_1) Gd_2O_3-MS NSs per milliliter and (*ii*) NS-free agarose (slice 4) were taken during PTT with a FLASH sequence. TR = 577 ms, TE = 6 ms, number of averages = 1, FA = 35°, FOV = 35 mm, matrix size = 128 × 128, slice thickness = 1.5 mm, and spacing between slices = 1.75 mm (scale bar = 2.6 mm).

changes in temperature can lead to a phase change in the MR images; the temperature change at an image N from the baseline ($T_N - T_1$) is a function of the phase change ($\delta\phi$) based on the relationship in Eq. 2 (8):

$$T_N - T_1 = \sum_{i=1}^{N} T_i - T_{i-1} = \frac{\sum_{i=1}^{N} \delta\phi_i}{2\pi \cdot \gamma B_0 \cdot \alpha \cdot TE}, \qquad [2]$$

where α is an assumed temperature sensitivity (−0.01 ppm/°C), and TE is the sequence echo time (6 ms). The proton resonance frequency (ω_1) is the product of γ the gyromagnetic ratio (42.58 MHz/T for hydrogen) and B_0 magnetic-field strength (4.7 T) (8). The samples discussed earlier (*SI Appendix*, Fig. S7) were used for this study. A 10-mm diffuser tip delivered an 810-nm illumination source with a uniform power density across the NMR tubes while monitoring the temperature change with thermal MRI mapping performed under 4.7-T magnetic strength (Fig. 4*A*). Before laser illumination, T_1w and T_2w MR images were acquired to localize the treatment and establish thermal-image planes. Fig. 4*B* shows a coronal T_1w MRI for one of the NMR tubes with the relevant axial slices set for thermal MRI measurements to monitor the temperature change during laser illumination. The superscript images (Fig. 4*B*, *i* and *ii*) are axial T_1w MR images of slices 2 and 4, respectively, across the NMR tubes at 2k-PEGylated Gd_2O_3-MS NS locations and NS-free agarose medium. A series of 14 T_1w MR images were acquired (73 s per image) to monitor and control the laser treatment in real time. This set of images covered a baseline, 3 min of 810-nm illumination at 4 W/1 W, and temperature recovery measurements. The T_1w MR images were processed with a MATLAB code to generate a thermal map for any plane of interest. For instance, Fig. 5*A* is a thermal map obtained from the last fast-low-angle-shot (FLASH) image acquired before the laser was turned OFF, presenting the maximum temperature change at the 2k-PEGylated Gd_2O_3-MS NS location after 3 min of continuous NIR illumination at 4 W. The highest temperature change (30 °C ≤ ΔT_{max} ≤ 54 °C) at the 2k-PEGylated Gd_2O_3-MS NS locations was achieved close to the illumination source (Fig. 5*A*). Fig. 5*B* represents the temperature change profile in real time during MR thermometry at three regions of interest: 1) 2k-PEGylated Gd_2O_3-MS NSs with 8.4 × 10^9 NSs per milliliter (red), 2) NS-free medium (green, ~2 m below the 2k-PEGylated Gd_2O_3-MS NSs band in the same NMR tube), and 3) reference (black, water), reaching a maximum temperature change of 51 ± 3 °C, 22 ± 1 °C, and 4 ± 1 °C (mean ± SD), respectively. Upon laser illumination, a rapid increase in the temperature (17 °C/min at 4 W, 5 °C/min at 1 W) was detected at a 2k-PEGylated Gd_2O_3-MS NS concentration of 8.4 × 10^9 NSs per milliliter (Fig. 5*B* and *SI Appendix*, Fig. S9). The reference sample was set far from the illumination source, revealing a minor increase in the temperature (ΔT_{max} = 4 ± 1 °C), which could be due to prolonged magnet exposure during the measurements.

Increasing 2k-PEGylated Gd_2O_3-MS NS concentrations from 1.1 × 10^9 to 2.1 × 10^9 2k-PEGylated Gd_2O_3-MS NSs per milliliter has statistically significantly increased the temperature change by ~1.5-fold (*P* value <0.001 at 4 W and <0.05 at 1 W). Nevertheless, temperature changes at 2k-PEGylated Gd_2O_3-MS NS concentrations >2.1 × 10^9 Gd_2O_3-MS NSs per milliliter were statistically insignificant at both laser powers

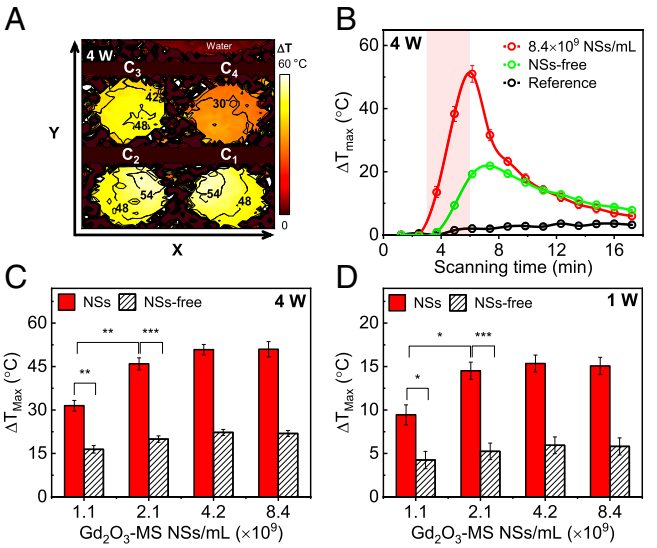

Fig. 5. Temperature change measurements with thermal MRI method at 4.7 T of various concentrations of 2k-PEGylated Gd_2O_3-MS NSs (27.5-nm gold shell) in 0.48% agarose phantoms under 3 min of 810-nm illumination at 4 W/1 W. (*A*) Maximum temperature changes across the four NMR tubes at the 2k-PEGylated Gd_2O_3-MS NS locations (slice 2 in Fig. 4*B*, *XY* plane), consisting of 1.1 × 10^9 (C_4), 2.1 × 10^9 (C_3), 4.2 × 10^9 (C_2), and 8.4 × 10^9 (C_1) Gd_2O_3-MS NSs per milliliter. The thermal MRI mapping was obtained using a MATLAB code by processing the last T_1w MRI collected before the laser illumination was turned OFF. (*B*) Temperature change profile during the treatment of three areas of interest: 2k-PEGylated Gd_2O_3-MS NSs with 8.4 × 10^9 NSs per milliliter (red, slice 2), ~2 mm below the 2k-PEGylated Gd_2O_3-MS NSs where the agarose medium was NS-free (green, slice 4), and the controlled measurements–Milli-Q water (black, slice 2). Each data point at time *x* represents the maximum temperature change calculated based on the phase change in T_1w MR image collected at time *x* relative to the first T_1w MR image. A two-dimensional fast-low-angle-shot (FLASH) gradient-echo scanning sequence was used to acquire time series of 14 T_1w images, 1 min and 13 s per scan. Solid lines are a guide to the eye. The red shaded area represents the illumination phase; its left side is the baseline phase, and its right side is the recovery phase. (*C* and *D*) Maximum temperature changes reached at the 2k-PEGylated Gd_2O_3-MS NS locations with various concentrations and NP-free agarose (~2 mm below the 2k-PEGylated Gd_2O_3-MS NSs band) after 3 min of NIR illumination at 4- and 1-W laser powers, respectively (***P < 0.0001, **P < 0.001, *P < 0.05 utilizing ANOVA with Tukey's honestly significant difference post hoc test). Error bars represent ± SE.

(Fig. 5*C* and *D*, red columns). This observation was consistent with previous reports within the same range of concentrations ($\geq 4 \times 10^9$ NSs per milliliter) (47). At 4 W (1 W), a maximum temperature change of 51 ± 3 °C (15 ± 1 °C) was reached for 2k-PEGylated Gd_2O_3-MS NSs with 4.2×10^9 and 8.4×10^9 2k-PEGylated Gd_2O_3-MS NSs per milliter concentrations, while 31 ± 2 °C (9 ± 1 °C) was achieved for the lowest concentration (1.1×10^9 2k-PEGylated Gd_2O_3-MS NSs per milliter). An additional slice was used to monitor the temperature of NS-free agarose medium, ∼2 mm lower than the 2k-PEGylated Gd_2O_3-MS NS band, weakly increasing with temperature due to the temperature increases at the nearby 2k-PEGylated Gd_2O_3-MS NS band, reaching a maximum temperature change of 22 ± 1 °C at 4 W and 6 ± 1 °C at 1 W (Fig. 5*C* and *D*, hatched columns). As soon as the illumination source was turned OFF, it took about 4 min for the temperature to go down and equilibrate with the surrounding NS-free agarose medium (Fig. 5*B* and *SI Appendix*, Fig. S9).

Discussion

PEGylated Gd_2O_3-MS NSs have a dual T_1/T_2 MRI contrast and a strong plasmon resonance in the NIR region where tissue is highly transparent (known as the first NIR therapeutic window), ideal for MRI-guided localized NIR-photothermal therapy. Previous reports have highlighted the potential of Gd_2O_3 to provide multiple-imaging capabilities, including fluorescence lifetime imaging (Gd^{3+} shortens the luminescence lifetime in the CNE-2 cell line) (48), X-ray–computed tomography (CT) (Gd has a higher X-ray attenuation/absorption coefficient than that of iodine—a commercial CT agent) (49), and MR imaging (Gd_2O_3 NP enhances the longitudinal proton relaxation rate [r_1] in comparison to chelated Gd^{3+} complexes) (39, 48, 49). Mesoporous silica is an ideal carrier platform for a large load of Gd_2O_3 NPs to increase their effect on the longitudinal water proton relaxivity for better MR imaging (38, 48, 50). Trapping Gd_2O_3 within the MS pores and attaching gold seeds on the silica surface have statistically significantly improved their r_1 and r_2 relaxivity values (P value <0.01) by 1.2× and 4.4×, respectively (Fig. 2*F* and *G*). This could be due to a large number of gadolinium atoms per nanoshell, the decrease in the tumbling rate of the 2k-PEGylated Gd_2O_3-MS structure (τ_R) (46), and the increase in the water exchange rate (τ_m) that was caused by the confinement space created by the channels and the pores within the structure(43). Forming a continuous gold shell and increasing its thickness have increased the distance between the Gd^{3+} and the water protons, decreasing the relaxivity rates as predicted by SBM theory (Fig. 2*H*). On the other hand, forming a gold shell and functionalizing its surface with PEG slows down the tumbling rate of the 2k-PEGylated Gd_2O_3-MS structure even further, increasing the relaxivity rates. The final Gd_2O_3-MS NS (Au ≤ 27.5 nm) has a statistically significantly higher r_1 relaxivity value than conventional agents (3.6× r_1 relaxivity rate of Magnevist, P value <0.001) and other multilayer-gold NPs (4.2× r_1 relaxivity rate of Gd-DOTA–doped nanomatryoshkas with a 22-nm gold shell thickness (46), which is due to an order of magnitude more Gd^{3+} per NP in Gd_2O_3-MS NS. This result makes 2k-PEGylated Gd_2O_3-MS NSs a better alternative as a T_1 CA. Furthermore, 2k-PEGylated Gd_2O_3-MS NSs have a comparable r_2 relaxivity rate to superparamagnetic iron oxide (SPIO) T_2 CAs ($r_{2\ \text{Ferumoxide}} = 105\ \text{mM}_{\text{Fe}}^{-1}\cdot\text{s}^{-1} < r_{2\ \text{2k-PEGylated Gd2O3-MS NSs}} < r_{2\ \text{Resovist}} = 176\ \text{mM}_{\text{Fe}}^{-1}\cdot\text{s}^{-1}$) (41) (Fig. 2*F* and *G*). Thus, 2k-PEGylated Gd_2O_3-MS NSs could be a potential candidate for T_1/T_2 dual-model MRI CAs. Nanoparticles with T_1/T_2 dual MRI have increased interest since they can provide accurate diagnostic information in T_1w and T_2w MR images. Most reported T_1/T_2 dual-mode MRI CAs consist of SPIO as a T_2 CA and (Gd^{3+}) (51–56) or (Fe^{3+}) (57, 58) as a T_1 CA. However, unlike these structures, our unique 2k-PEGylated Gd_2O_3-MS NS nanoparticle behaves as a T_2 CA despite lacking SPIO NPs.

We believe that our structure has a strong r_2 relaxivity rate since when multiple domains of paramagnetic material such as Gd_2O_3 are concentrated within a single structure, as in 2k-PEGylated Gd_2O_3-MS NSs, it may be possible that the entire 2k-PEGylated Gd_2O_3-MS NS structure starts to behave as a superparamagnetic material. Multiple domains of Gd_2O_3 in a single 2k-PEGylated Gd_2O_3-MS NS will increase the susceptibility of the 2k-PEGylated Gd_2O_3-MS NSs, making them more magnetic when placed in an external magnetic field, improving the 2k-PEGylated Gd_2O_3-MS NSs interaction with the external magnetic field, causing the magnetic lines to be even more concentrated within the 2k-PEGylated Gd_2O_3-MS NSs. This increases the local magnetic-field differences and causes the 2k-PEGylated Gd_2O_3-MS NSs to appear to have superparamagnetic properties. This reported behavior requires further investigation in future studies. Unlike T_1 relaxation time, T_2 relaxation time is sensitive to local changes in the magnetic field. The more perturbation there is within the local magnetic field, each spin will experience different local magnetic fields, causing them to precess at various frequencies, increasing decoherence and inhomogeneity in the transverse plane, and eventually, a faster decay of the transverse magnetization is detected. This could explain the 4.4-fold statistically significant enhancement in the r_2 of 2k-PEGylated Gd_2O_3-MS NSs with a 22.3-nm gold shell relative to Gd_2O_3 nanocrystals (P value = 0.0000).

The MRI properties with time depended on the stage of the synthesized nanoparticles caused by the rearrangement of the gold atoms as a function of time (*SI Appendix*, Fig. S6). When the Au-seeded Gd_2O_3-MS or Gd_2O_3-MS NSs with a 22.3-nm Au shell were synthesized, long channels may have formed, creating more confined space for the water molecule, resulting in high relaxivity values. However, rearrangement of Au atoms with time may have blocked channels, preventing the fast exchange of water molecules with the Gd-contrast agent inside the MS core. As a result, the r_1 and r_2 and r_2/r_1 values were statistically significantly decreased to 15.6 ± 0.3 $\text{mM}_{\text{Gd}}^{-1}\cdot\text{s}^{-1}$, 64 ± 2 $\text{mM}_{\text{Gd}}^{-1}\cdot\text{s}^{-1}$, and 4.4 ± 0.1, respectively, for Au-seeded 2k-PEGylated Gd_2O_3-MS 7 wks postsynthesis. Furthermore, the r_1 and r_2 for 2k-PEGylated Gd_2O_3-MS NSs with a 22.3-nm Au shell have statistically significantly decreased to 10.2 ± 0.6 $\text{mM}_{\text{Gd}}^{-1}\cdot\text{s}^{-1}$ and 80 ± 1 $\text{mM}_{\text{Gd}}^{-1}\cdot\text{s}^{-1}$, respectively, while no statistically significant difference was observed in their r_2/r_1 value with time. In the scenario of thicker gold shells, 27.5-nm Au for instance, rearrangement of the Au atoms is expected to decrease the roughness of the NSs' surface area, which will cause a slight decrease in the distance between the water molecule and the Gd-contrast agent, causing a statistically significant enhancement in the r_1 and r_2 relaxivity values without a statistically significant difference in their r_2/r_1 ratio as a function of time. The rearrangement of gold atoms in the 2k-PEGylated Gd_2O_3-MS NSs with 22.3 and 27.5 nm Au shell thicknesses has given a final r_1 relaxivity value (∼10 $\text{mM}_{\text{Gd}}^{-1}\cdot\text{s}^{-1}$) still higher than that of Magnevist and a final r_2 relaxivity value (∼80 $\text{mM}_{\text{Gd}}^{-1}\cdot\text{s}^{-1}$) still comparable with that of the SPIO-contrast agent. Even though 2k-PEGylated Gd_2O_3-MS NSs have statistically significant lower r_1 and r_2 values 7 wk postsynthesis, their r_2/r_1 ratio changes were statistically insignificant (*SI Appendix*, Fig. S6).

We found the average relative intensity of the four samples obtained with the T_1/T_2 ratio (TE = 425 ms) was statistically significant at the 0.5 level in comparison with T_1w (P value = 0.2515) or T_1/T_2 ratio with TE = 83 ms (P value = 0.2715) due to T_2w MRI high sensitivity to noise at long echo times (Fig. 3*E* and *F*). The enhancement in the signal intensity of the T_1w/T_2w ratio has been reported previously to improve the detection and localization of cortical lesions by enhancing the contrast to noise ratio between heavily and lightly myelinated areas in the cortical surface (35–37, 59). That was possible because the high myelin content of a cortical site gives high and low signal intensities in T_1w MRI and T_2w MRI, respectively. Gd_2O_3-MS NSs behave as myelin by enhancing the signal in T_1w MRI sequences and suppressing that in T_2w MRI sequences, resulting in a better contrast MRI with T_1w/T_2w signal intensity ratio. This report presents an MRI CA capable of enhancing contrast by processing the T_1w/T_2w ratio.

Promising Gd-based MRI active theranostic nanomaterials have been developed combining imaging and PTT, including a gold nanorod coated with Gd-chelate or with a Gd_2O_3 loaded mesoporous silica layer (60, 61). Unlike in those structures, the Gd_2O_3 crystals in Gd_2O_3-MS NSs are coated with a continuous gold shell, which decreases their likelihood of getting released to the surroundings and causing toxicity. Moreover, applying the same illumination conditions as have been used in clinical trials (3 min with 810 nm at 4 W with a 10-mm diffuser tip) has caused excessive thermal damage, causing a statistically significant increase in temperature ($32\,°C < \Delta T < 51\,°C$) at the Gd_2O_3-MS NSs location with (1.1 to 8.4) $\times 10^9$ Gd_2O_3-MS NSs per milliliter versus at the nearby NP-free agarose phantom ($\Delta T \sim 16$ to $22\,°C$, P value < 0.001; Fig. 5*C*). In vivo, reaching a temperature $\geq 49\,°C$ ($\Delta T = 12\,°C$) would be sufficient to induce thermal damage by necrosis even in NS-free tissue regions, as it would be expected to destroy the cell membrane, secrete the cytoplasm to the extracellular part, and induce inflammation (22). Thus, reducing laser power to levels below what has been used in clinical studies was critical for minimal thermal heating of the NS-free agarose medium. Decreasing the laser power to 1 W was sufficient to cause statistically significant thermal heating at the Gd_2O_3-MS NS locations ($9\,°C < \Delta T < 15\,°C$) in an agarose phantom while causing minimum thermal heating to the NS-free agarose phantom ($\Delta T_{max} = 5\,°C$, P value < 0.05). These temperature changes are expected to initiate apoptosis (23) and necroptosis (24–26), ideal for tumor thermal ablation while sparing healthy tissue. A minimum concentration of 2.1×10^9 Gd_2O_3-MS NSs per milliliter was found to statistically cause significant thermal heating under 810 nm of illumination at 1 W ($\Delta T_{max} = 15 \pm 1\,°C$) in agarose phantoms while sparing the nearby NS-free medium ($\Delta T_{max} = 5 \pm 1\,°C$, P value ≤ 0.0001; Fig. 5*D*). Nevertheless, the conditions (NSs dosage, route of administration, and laser power) need to be further optimized in future in vivo studies for effective Gd_2O_3-MS NSs-induced photothermal therapy under MRI guidance.

With dual-MRI contrast and NIR photothermal properties, our Gd_2O_3-MS NSs system can provide MRI-guided localized NIR-PTT treatment that could increase cancer patients' survival rate. This study demonstrates a valuable dual-function capability that could be quickly translated into clinical use since gold NSs and NIR laser ablation protocols are Food and Drug Administration approved. This would allow illumination conditions (illumination time and laser power) to be conducted and optimized in future studies to avoid excessive/partial treatment and minimize thermal damage to NP-free tissue. These nanoparticles' quantitative measurements will enable quantitative theoretical thermal models of PTT that can predict the best combination of NS concentration, illumination time, and excitation power for optimizing treatment protocols and guaranteeing optimal photothermal therapy outcomes.

Methods

BET nitrogen adsorption/desorption isotherm measurements and BET data were used to determine the surface area of dry MS and its pore size. TEM measurements were conducted to determine the size distribution and morphology of the material at each step of Gd_2O_3-MS NS synthesis. STEM-HAADF images and energy-dispersive X-ray element mapping were used for elemental analysis. Inductively coupled plasma mass spectroscopy (ICP-MS) was used to determine the concentrations of elements, mainly Gd^{3+}, within samples. MRI at 4.7 T was used to obtain the spin–lattice relaxation (T_1) and spin–spin relaxation (T_2) time constants for PEGylated Gd_2O_3-MS NS suspensions. The R_1 ($1/T_1$) and R_2 ($1/T_2$) relaxation rate constants were plotted versus the gadolinium concentration in (mM_{Gd}) to obtain the r_1 and r_2 relaxivities ($mM_{Gd}^{-1} \cdot s^{-1}$) of the PEGylated Gd_2O_3-MS NS at a different stage of synthesis. MRI was also used to collect T_1- and T_2-weighted MR images for thermal MRI mapping measurements to evaluate the phase change caused by temperature change during photothermal treatment. A Diomed laser (CW-GaAlAs, 810 ± 20 nm) was used to deliver energy to the samples to a targeted location with an optical SMA-905–type connector output (400 μm, 0.37 NA). The laser output was coupled into a Visualase laser diffusing fiber (12 m long, 400 μm core diameter, and 10 mm diffusing tip length) (Fig. 4*A*, *i* and *SI Appendix*, Fig. S9). The diffuser tip was placed in a tube, aligned symmetrically relative to the four samples of NMR tubes, and secured with adhesive tape to restrict its movement relative to the samples during the MRI measurements (*SI Appendix*, Fig. S7).

Reagents. Ethanol (200 proof) was purchased from Decon Laboratories, Inc. From Sigma-Aldrich, the following were purchased: CTAB (≥99%), ammonium hydroxide solution (28% NH_3 in water), tetraethyl orthosilicate (TEOS) (≥99.9%), acetone (≥99.5%), gadolinium(III) chloride hexahydrate ($GdCl_3 \cdot 6H_2O$) (99%), diethylene glycol (DEG) (99%), (3-aminopropyl)-triethoxysilane (APTES) (99%), sodium chloride (NaCl) (≥99%), and tetrakis(hydroxymethyl) phosphonium chloride (THPC) (80% in water). A total of 1 wt% chloroauric acid solution was prepared by suspending 5 g of Gold(III) chloride trihydrate (≥99.9%) from Sigma-Aldrich in 500 mL Milli-Q water. The chloroauric acid solution was aged for at least 1 mo before use. Formaldehyde solution (CH_2O) (31%) was purchased from Macron Fine Chemicals. Methoxy PEG Thiol (mPEG-SH) (MW = 2,000) was purchased from Laysan Bio, Inc. Multielement internal standard (2 wt% HNO_3, 10 mg/L Ho) were purchased from Atomic Spectroscopy. Gadolinium ICP/DCP standard solution (10,006 μg/mL in 2 wt% HNO_3) and hydrochloric acid (HCl) (≥30%) were purchased from Fluka Analytical. Sodium hydroxide solution (NaOH) (1 N), potassium carbonate anhydrous (K_2CO_3) (≥99%), and nitric acid (HNO_3) (70%) were purchased from Fisher Chemical. Aqua regia (HNO_3/HCl [vol/vol], 1:3) was used to clean laboratory glassware and stir bars, followed by thorough rinsing with deionized water. Milli-Q water (18.2 MΩ·cm at 25 °C; Millipore) was used during all of the reactions and the last step of glassware washing.

MS Synthesis. The porosity of silica can be tuned by changing reaction parameters, mainly the CTAB/tetraethoxysilane (TEOS) molar ratio and the ethanol/water volume ratio (62). NPs were prepared based on a published procedure with minor modifications (1.33 molar ratio of CTAB/TEOS and 0.43 volume ratio of ethanol/water) (38). Briefly, 0.383 g of CTAB, which acted as the structure-directing agent, was mixed with 175 mL Milli-Q water at 30 to 35 °C in a 500-mL closed round bottom flask connected to a condenser to avoid solution depletion until the CTAB was completely dissolved. Under stirring conditions, 75 mL of 200-proof ethanol was added for a 250-mL final synthesis volume followed by the addition of 300 μL of ammonia (28 vol%) as the catalyst to reach a pH of 10, followed by 200 μL of TEOS as silica source. The TEOS solution was added dropwise under continuous stirring to grow particles with a narrow size distribution. The reaction was run at 60 °C for 3 d. The reaction was cooled down to room temperature while continuously being stirred to avoid particle aggregation. The particles were recovered by centrifuging a 10-mL sample in a 50-mL

centrifuge tube for 15 min at 18,000 × *g* and 25 °C. The collected pellet was dispersed in ethanol with mild sonication followed by three centrifugation cycles to remove free TEOS. Then, the final pellet was dispersed in ∼1 mL of water and baked at 500 °C for 4 h to remove the CTAB template (*SI Appendix*, Fig. S1). The final white solid material of mesoporous silica was dispersed in 5 mL of Milli-Q water through vigorous sonication. This solution was mixed with Gd_2O_3 NPs solution under 4 h of sonication to load Gd_2O_3 into the mesoporous silica pores.

Gd_2O_3 Synthesis. The Gd_2O_3 synthesis was performed under an argon environment attached to the condensation system to better control the oxidation process. Briefly, 5.8 g of gadolinium chloride hexahydrate was dissolved in 100 mL of diethylene glycol in a 250-mL round bottom flask. The solution was set at 60 °C and stirred overnight. On the following day, 22.5 mL of (1 M) NaOH was added quickly and vigorously stirred at 750 rpm while the temperature was increased to 140 °C at 5 °C/min ramping rate (RR). After 1 h of reaction at 140 °C, the temperature was increased to 180 °C (RR = 4 °C/min) and was run for another 4 h. The final product was a transparent colloid solution of Gd_2O_3 NPs. The suspension of Gd_2O_3 was cooled down to room temperature and stored at 4 °C, ready to be mixed with MS aqueous suspension (*SI Appendix*, Fig. S2).

The 2k-PEGylated Gd_2O_3-MS NSs Synthesis. The synthesis of the final 2k-PEGylated Gd_2O_3-MS NSs involved multiple sequential processes, including 1) preparation of Gd_2O_3-MS and surface amination, 2) preparation of 1- to 3-nm gold NPs, 3) attachment of 1- to 3-nm gold NPs on the aminated Gd_2O_3-MS, and 4) formation of a continuous shell of gold and NSs surface PEGylation (see *SI Appendix* for more details).

Calculation of Gd^{3+} Concentration per Gd_2O_3-MS NS Structure. The concentration of Gd atoms per Gd_2O_3-MS NS structure was calculated by determining the molar concentration of Gd^{3+} from ICP-MS analysis and the molar concentration (*c*) of NSs based on Beer's law (*SI Appendix*, Eq. **S1**). A fixed core diameter size of 95 nm and a shell thickness distribution with an average of 25 nm were needed in the theoretical model to best fit the absorbance of an aqueous suspension of (2k) PEGylated Gd_2O_3-MS NSs. *SI Appendix*, Fig. S10 shows an example of such a fitting, giving 3.63×10^{-13} mol/L as the NSs' molar concentration. Using ICP-MS analysis, the molar concentration of Gd^{3+} for that sample was found to be 1.218×10^{-6} mol/L, giving 3.4×10^6 Gd^{3+}/NS. The Gd^{3+} molar concentration was determined for other samples, providing an average value of $(3.3 \pm 0.1) \times 10^6$ Gd^{3+}/NS for Gd_2O_3-MS NSs nanostructure.

Evaluation of r_1 and r_2 Relaxivity Values MRI of Samples. The MRI studies were performed using a 4.7-T scanner (Bruker BioSpec USR 47/40) with a 12-cm gradient insert and a volume resonator with a 72-mm inner diameter; even though this scanner is not clinically relevant at 1.5 and 3 T, it was utilized so that the MRI properties of our particles can be directly compared with other nanostructures developed in our laboratory that were characterized with the 4.7 T scanner. A series of dilutions of an aqueous suspension of PEGylated Gd_2O_3-MS NSs were prepared (100 μL each in 150-μL Eppendorf tubes). The samples were placed in a customized transparent container (*SI Appendix*, Fig. S5) that allowed the samples to be surrounded by an aqueous solution to remove the air–water interface and suppress the susceptibility effect it could cause. The sample holder was placed in the center of the 72-mm inner diameter excitation coil at room temperature (21 °C). T_1 maps were generated from saturation recovery data acquired using a rapid-acquisition refocused-echo (RARE) spin–echo sequence that loops across a range of repetition time values. The imaging parameters were as follows: TE = 9.94 ms; TR array = 27.3, 400, 851, 1,403, 2,113, 3,107, 4,782, and 12,500 ms; RARE factor = 2; image matrix = 84 × 84; and total scan time for each T_1 map = 13 min and 25 s. T_2 maps were generated from a multislice–multiecho (MSME) spin–echo sequence that acquires imaging data across a range of echo times. Paravision version 5.1 was used to fit the magnetization recovery signals at various TR values and the dephasing signals at various TE values with Eq. 1 to calculate the T_1 and T_2 relaxation times, respectively, for various samples. The imaging parameters were as follows: TE range = 8.6 to 829 ms, echo spacing = 8.6369 ms, TR = 1,750 ms, image matrix = 128 × 128, and total scan time = 2 min and 48 s. A slice thickness = 3 mm, field of view (FOV) = 55 × 55 mm, and a number of signal averages = 1 were identical in both datasets.

Theoretical r_1 Relaxivity Value Prediction Using SBM Theory. SBM theory (39, 63, 64) was utilized to estimate the r_1 relaxivity of the NSs. As Gd_2O_3 particles are embedded within the NSs away from the water molecules, only outer sphere contributions (43) are considered in the r_1 relaxivity calculation according to *SI Appendix*, Eq. **S2**. An average diameter of 95 nm of the MS core was used in the calculation in addition to Gd^{3+} concentration per NS (3.3×10^6 Gd^{3+}/NS) that was determined earlier. As Gd_2O_3 particles are distributed unevenly in the MS core, an uneven distribution was implemented to estimate the final result (46). In practice, the best fitting to experimental results was achieved when 50% of the Gd_2O_3 particles are near the surface, while the other 50% were distributed uniformly inside the core.

ICP-MS Measurements. The concentration of Gd within samples was evaluated using ICP-MS. The measurements were performed using a Perkin-Elmer Nexion 300 ICP-MS. Initially, 25 μL of each sample was digested in 200 μL concentrated aqua regia and left overnight with a loss cover. The resulting solutions were diluted on the next day with 2% vol/vol nitric acid (HNO_3) 400 times. Furthermore, various gadolinium ICP/DCP standard solution concentrations with 1, 10, 100, and 1,000 μg/L were prepared to generate a calibration curve. Internal standard (Ho 165) was added to all samples, gadolinium standard solutions, and a blank solution and kept its final concentration the same (15 μg/L) to ensure no changes within the instrument detection sensitivity occurred during the measurements.

Sample Preparation, T_1w/T_2w Ratio Image Processing, and Photothermal Treatment under Thermal MRI Guidance.

Sample preparation. Four NMR tubes were prepared with a 40-μL layer of k-PEGylated Gd_2O_3-MS NSs (27.5 ± 0.1 nm Au shell) with 1.1×10^9, 2.1×10^9, 4.2×10^9, and 8.4×10^9 Gd_2O_3-MS NSs per milliliter in 0.48% agarose surrounded with 0.8% agarose suspension. The NMR tubes were placed in a square shape with an empty tube in the middle to position and center the diffuser optical fiber with an equal distance from all samples and the same laser power density exposure. A control sample, NS-free DI water, was placed on the NMR tubes.

T_1w/T_2w ratio image processing. Before laser illumination, T_1w and T_2 wweighted MR images were acquired to determine the relaxivity rate stability with time in the agarose phantom and to obtain the best T_1w and T_2w images with the highest signal contrast. A series of T_1-weighted MR images were collected with the following imaging parameters: TE = 9.94 ms; TR array = 194, 577, 1,028, 1,580, 2,288, 3,281, 4,952, and 12,500 ms; RARE factor = 2; and total scan time for each T_1 map = 21 min and 7 s. T_2w MR images were measured with MSME sequence with the following imaging parameters: TE range = 9.2 to 443.9 ms, echo spacing = 9.2489 ms, TR = 3,857 ms, and total scan time = 8 min and 13 s. A slice thickness = 1.5 mm, image matrix = 128 × 128, FOV = 35 × 35 mm, and the number of signal averages = 1 were identical in both datasets. Eq. 1 was used to fit the magnetization recovery signals at various TR values and the signal decay at various TE to obtain T_1 and T_2 relaxation times, respectively, for various samples. T_1- and T_2- signal contrast plots were achieved by subtracting the normalized signal of the reference (water) from the 2k-PEGylated Gd_2O_3-MS NSs samples (*SI Appendix*, Fig. S8), resulting in Fig. 3*A* and *B*. Afterward, the T_1w and T_2w MR images that have given the optimum signal contrast were selected for T_1w/T_2w ratio image processing by taking the ratio of their signal intensities.

Photothermal treatment conditions and thermal MRI mapping. An 810-nm Diomed laser coupled with a 10-mm diffusing tip was used to illuminate the samples for 3 min at 4 W/ 1W. The treatments were performed on a 4.7-T MR scanner and monitored with magnetic resonance thermal imaging (MRTI), which was established based on the temperature-dependent proton resonance frequency (PRF) method (65–67) with temperature accuracies of ±0.2 °C (65). A two-dimensional (2D) FLASH gradient echo scanning sequence was used to acquire time series of 14 T_1w images, 1 min and 13 s per scan. The temperature-sensitive imaging across the four NMR tubes was achieved with 128 × 128 matrix size, 1.5-mm slice thickness, 1.75-mm spacing between slices, 0.27-mm spatial resolution, 577 ms TR, 6 ms TE, and 35° flip angle. The acquired voxel size was $0.28 \times 0.28 \times 1.5$ mm^3. A total scan of 17 min and 13 s was sufficient to cover a baseline, 3 min of laser illumination at 4 W/ 1W, and recovery measurements of temperature change. T_1w and T_2w scout MR images were performed before the treatment to align the sample and the laser fiber and establish the thermal imaging plane. The same MR images were acquired after the treatment

to ensure no changes within the sample, such as bubble formation, have occurred during the measurements. MRI data processing and thermal mapping plotting were acquired offline using OriginPro 2021b and a code developed with MATLAB.

Data Availability. Some study data are available upon request. The MATLAB code will be provided to readers upon request.

ACKNOWLEDGMENTS. We especially thank the Shared Equipment Authority at Rice University for providing equipment (TEM, HR-TEM, and ICP-MS) critical for this study. We especially thank Dr. Christopher Pennington for training on the ICP-MS and Dr. Wenhua Guo for his assistance in HR-TEM measurements during COVID-19. We thank the Imaging Research Facility at the Department of Imaging Physics at M. D. Anderson Cancer Center, especially Mrs. Kiersten Maldonado, for her assistance in taking MR images during COVID-19. This work was financially supported by an M. D. Anderson/Rice Postdoctoral T32 Fellowship in Translational Cancer Nanotechnology (T32CA196561), the Robert A. Welch Foundation (C-1220 to N.J.H. and C-1222 to P.J.N.), and the Carl and Lillian Illig Fellowship (Smalley-Curl Institute, H20398-239440).

1. A. R. Rastinehad *et al.*, Gold nanoshell-localized photothermal ablation of prostate tumors in a clinical pilot device study. *Proc. Natl. Acad. Sci. U.S.A.* **116**, 18590–18596 (2019).
2. N. K. Jain *et al.*, Nanoengineered photoactive theranostic agents for cancer. *Nanophotonics* **10**, 2973–2997 (2021).
3. R. Weissleder, A clearer vision for in vivo imaging. *Nat. Biotechnol.* **19**, 316–317 (2001).
4. A. M. Smith, M. C. Mancini, S. Nie, Bioimaging: Second window for in vivo imaging. *Nat. Nanotechnol.* **4**, 710–711 (2009).
5. D. E. Hudson, D. O. Hudson, J. M. Wininger, B. D. Richardson, Penetration of laser light at 808 and 980 nm in bovine tissue samples. *Photomed. Laser Surg.* **31**, 163–168 (2013).
6. N. S. Abadeer, C. J. Murphy, Recent progress in cancer thermal therapy using gold nanoparticles. *J. Phys. Chem. C* **120**, 4691–4716 (2016).
7. R. J. Stafford *et al.*, MR temperature imaging of nanoshell mediated laser ablation. *Int. J. Hyperthermia* **27**, 782–790 (2011).
8. L. R. Hirsch *et al.*, Nanoshell-mediated near-infrared thermal therapy of tumors under magnetic resonance guidance. *Proc. Natl. Acad. Sci. U.S.A.* **100**, 13549–13554 (2003).
9. S. R. Aglyamov, S. Y. Emelianov, J. Shah, K. Sokolov, T. E. Milner, Ultrasound-based thermal and elasticity imaging to assist photothermal cancer therapy–Preliminary study. *Proc. IEEE Ultrason. Symp.* 1, 1029–1032 (2006).
10. J. Shah *et al.*, Photoacoustic imaging and temperature measurement for photothermal cancer therapy. *J. Biomed. Opt.* **13**, 034024 (2008).
11. L. Meng *et al.*, Photoacoustic temperature imaging based on multi-wavelength excitation. *Photoacoustics* **13**, 33–45 (2018).
12. R. Castelino, W. Whelan, M. Kolios, *Photoacoustic Detection of Protein Coagulation in Albumen-Based Phantoms* (SPIE, 2008).
13. M. R. Bailey, V. A. Khokhlova, O. A. Sapozhnikov, S. G. Kargl, L. A. Crum, Physical mechanisms of the therapeutic effect of ultrasound (a review). *Acoust. Phys.* **49**, 369–388 (2003).
14. Y. Cheng, S. Li, R. J. Eckersley, D. S. Elson, M. X. Tang, Detecting tissue optical and mechanical properties with an ultrasound modulated optical imaging system in reflection detection geometry. *Biomed. Opt. Express.* **6**, 63–71 (2014).
15. S. S. Salami *et al.*, Multiparametric magnetic resonance imaging outperforms the Prostate Cancer Prevention Trial risk calculator in predicting clinically significant prostate cancer. *Cancer* **120**, 2876–2882 (2014).
16. J. A. Schwartz *et al.*, Feasibility study of particle-assisted laser ablation of brain tumors in orthotopic canine model. *Cancer Res.* **69**, 1659–1667 (2009).
17. P. C. Schulze, T. Kahn, T. Harth, H. J. Schwurzmaier, R. Schober, Correlation of neuropathologic findings and phase-based MRI temperature maps in experimental laser-induced interstitial thermotherapy. *J. Magn. Reson. Imaging* **8**, 115–120 (1998).
18. M. D. Sherar *et al.*, Comparison of thermal damage calculated using magnetic resonance thermometry, with magnetic resonance imaging post-treatment and histology, after interstitial microwave thermal therapy of rabbit brain. *Phys. Med. Biol.* **45**, 3563–3576 (2000).
19. M. Kangasniemi *et al.*, Thermal therapy of canine cerebral tumors using a 980 nm diode laser with MR temperature-sensitive imaging feedback. *Lasers Surg. Med.* **35**, 41–50 (2004).
20. R. J. McNichols *et al.*, MR thermometry-based feedback control of laser interstitial thermal therapy at 980 nm. *Lasers Surg. Med.* **34**, 48–55 (2004).
21. R. J. McNichols *et al.*, Technical developments for cerebral thermal treatment: Water-cooled diffusing laser fibre tips and temperature-sensitive MRI using intersecting image planes. *Int. J. Hyperthermia* **20**, 45–56 (2004).
22. P. Golstein, G. Kroemer, Cell death by necrosis: Towards a molecular definition. *Trends Biochem. Sci.* **32**, 37–43 (2007).
23. S. Elmore, Apoptosis: A review of programmed cell death. *Toxicol. Pathol.* **35**, 495–516 (2007).
24. D. E. Christofferson, J. Yuan, Necroptosis as an alternative form of programmed cell death. *Curr. Opin. Cell Biol.* **22**, 263–268 (2010).
25. L. Galluzzi, G. Kroemer, Necroptosis: A specialized pathway of programmed necrosis. *Cell* **135**, 1161–1163 (2008).
26. Z. Su, Z. Yang, L. Xie, J. P. DeWitt, Y. Chen, Cancer therapy in the necroptosis era. *Cell Death Differ.* **23**, 748–756 (2016).
27. P. X. E. Mouratidis, I. Rivens, G. Ter Haar, A study of thermal dose-induced autophagy, apoptosis and necroptosis in colon cancer cells. *Int. J. Hyperthermia* **31**, 476–488 (2015).
28. S. Parida *et al.*, Gold nanorod embedded reduction responsive block copolymer micelle-triggered drug delivery combined with photothermal ablation for targeted cancer therapy. *Biochim. Biophys. Acta Gen. Subj.* **1861** (1 Pt A), 3039–3052 (2017).
29. M. Pérez-Hernández *et al.*, Dissecting the molecular mechanism of apoptosis during photothermal therapy using gold nanoprisms. *ACS Nano* **9**, 52–61 (2015).
30. A. J. Gormley *et al.*, Gold nanorod mediated plasmonic photothermal therapy: A tool to enhance macromolecular delivery. *Int. J. Pharm.* **415**, 315–318 (2011).
31. A. J. Gormley *et al.*, Plasmonic photothermal therapy increases the tumor mass penetration of HPMA copolymers. *J. Control. Release* **166**, 130–138 (2013).
32. B. L. Fay, J. R. Melamed, E. S. Day, Nanoshell-mediated photothermal therapy can enhance chemotherapy in inflammatory breast cancer cells. *Int. J. Nanomedicine* **10**, 6931–6941 (2015).
33. M. P. Melancon *et al.*, Near-infrared light modulated photothermal effect increases vascular perfusion and enhances polymeric drug delivery. *J. Control. Release* **156**, 265–272 (2011).
34. M. Misaki *et al.*, Contrast enhancement by combining T_1- and T_2-weighted structural brain MR Images. *Magn. Reson. Med.* **74**, 1609–1620 (2015).
35. R. Righart *et al.*, Cortical pathology in multiple sclerosis detected by the T_1/T_2-weighted ratio from routine magnetic resonance imaging. *Ann. Neurol.* **82**, 519–529 (2017).
36. Y. F. Zheng *et al.*, Sensitivity of T_1/T_2-weighted ratio in detection of cortical demyelination is similar to magnetization transfer ratio using post-mortem MRI. *Mult. Scler. J.* **28**, 198–205 (2022).
37. M. F. Glasser, D. C. Van Essen, Mapping human cortical areas in vivo based on myelin content as revealed by *T1*- and *T2*-weighted MRI. *J. Neurosci.* **31**, 11597–11616 (2011).
38. K. Ni *et al.*, Geometrically confined ultrasmall gadolinium oxide nanoparticles boost the $T(_1)$ contrast ability. *Nanoscale* **8**, 3768–3774 (2016).
39. J. L. Bridot *et al.*, Hybrid gadolinium oxide nanoparticles: Multimodal contrast agents for in vivo imaging. *J. Am. Chem. Soc.* **129**, 5076–5084 (2007).
40. L. Faucher, M. Tremblay, J. Lagueux, Y. Gossuin, M. A. Fortin, Rapid synthesis of PEGylated ultrasmall gadolinium oxide nanoparticles for cell labeling and tracking with MRI. *ACS Appl. Mater. Interfaces* **4**, 4506–4515 (2012).
41. M. Rohrer, H. Bauer, J. Mintorovitch, M. Requardt, H. J. Weinmann, Comparison of magnetic properties of MRI contrast media solutions at different magnetic field strengths. *Invest. Radiol.* **40**, 715–724 (2005).
42. S. Caspani, R. Magalhães, J. P. Araújo, C. T. Sousa, Magnetic nanomaterials as contrast agents for MRI. *Materials (Basel)* **13**, 29 (2020).
43. J. S. Ananta *et al.*, Geometrical confinement of gadolinium-based contrast agents in nanoporous particles enhances *T1* contrast. *Nat. Nanotechnol.* **5**, 815–821 (2010).
44. P. Caravan, C. T. Farrar, L. Frullano, R. Uppal, Influence of molecular parameters and increasing magnetic field strength on relaxivity of gadolinium- and manganese-based T1 contrast agents. *Contrast Media Mol. Imaging* **4**, 89–100 (2009).
45. R. B. Lauffer, Paramagnetic metal-complexes as water proton relaxation agents for NMR imaging-theory and design. *Chem. Rev. (Washington, DC)* **87**, 901–927 (1987).
46. V. S. Marangoni *et al.*, Enhancing T_1 magnetic resonance imaging contrast with internalized gadolinium(III) in a multilayer nanoparticle. *Proc. Natl. Acad. Sci. U.S.A.* **114**, 6960–6965 (2017).
47. G. S. Terentyuk *et al.*, Laser-induced tissue hyperthermia mediated by gold nanoparticles: Toward cancer phototherapy. *J. Biomed. Opt.* **14**, 021016 (2009).
48. H. Wang *et al.*, High sensitivity of gold nanoparticles co-doped with Gd_2O_3 mesoporous silica nanocomposite to nasopharyngeal carcinoma cells. *Sci. Rep.* **6**, 34367 (2016).
49. M. W. Ahmad *et al.*, Potential dual imaging nanoparticle: Gd_2O_3 nanoparticle. *Sci. Rep.* **5**, 8549 (2015).
50. S. A. Li *et al.*, Mesoporous silica nanoparticles encapsulating Gd_2O_3 as a highly efficient magnetic resonance imaging contrast agent. *Appl. Phys. Lett.* **98**, 3 (2011).
51. Z. Zhou *et al.*, A synergistically enhanced $T(_1)$-$T(_2)$ dual-modal contrast agent. *Adv. Mater.* **24**, 6223–6228 (2012).
52. K. Cheng *et al.*, Hybrid nanotrimers for dual T_1 and *T*-weighted magnetic resonance imaging. *ACS Nano* **8**, 9884–9896 (2014).
53. S. Zheng *et al.*, Tumor-targeted Gd-doped mesoporous Fe_3O_4 nanoparticles for T_1/T_2 MR imaging guided synergistic cancer therapy. *Drug Deliv.* **28**, 787–799 (2021).
54. J. Li *et al.*, T_1-T_2 molecular magnetic resonance imaging of renal carcinoma cells based on nano-contrast agents. *Int. J. Nanomedicine* **13**, 4607–4625 (2018).
55. L. Y. Lai *et al.*, Gadolinium-chelate functionalized magnetic $CuFeSe_2$ ternary nanocrystals for T_1-T_2 dual MRI and CT imaging in vitro and in vivo. *Mater. Res. Express.* **8**, 10 (2021).
56. X. Sun *et al.*, A pH-responsive yolk-like nanoplatform for tumor targeted dual-mode magnetic resonance imaging and chemotherapy. *ACS Nano* **11**, 7049–7059 (2017).
57. J. Li *et al.*, Dual-mode avocado-like all-iron nanoplatform for enhanced T_1/T_2 MRI-guided cancer theranostic therapy. *Nano Lett.* **20**, 4842–4849 (2020).
58. G. Shu *et al.*, Sialic acid-engineered mesoporous polydopamine nanoparticles loaded with SPIO and Fe^{3+} as a novel theranostic agent for T1/T2 dual-mode MRI-guided combined chemo-photothermal treatment of hepatic cancer. *Bioact. Mater.* **6**, 1423–1435 (2020).
59. K. Nakamura, J. T. Chen, D. Ontaneda, R. J. Fox, B. D. Trapp, T_1-/T_2-weighted ratio differs in demyelinated cortex in multiple sclerosis. *Ann. Neurol.* **82**, 635–639 (2017).
60. J. Yin *et al.*, Nanoassembly and multiscale computation of multifunctional optical-magnetic nanoprobes for tumor-targeted theranostics. *ACS Appl. Mater. Interfaces* **11**, 41069–41081 (2019).
61. A. Pitchaimani *et al.*, Gd^{3+} tethered gold nanorods for combined magnetic resonance imaging and photo-thermal therapy. *J. Biomed. Nanotechnol.* **13**, 417–426 (2017).
62. Y. J. He, J. Li, M. Q. Long, S. Q. Liang, H. Xu, Tuning pore size of mesoporous silica nanoparticles simply by varying reaction parameters. *J. Non-Cryst. Solids* **457**, 9–12 (2017).
63. G. Mie, Articles on the optical characteristics of turbid tubes, especially colloidal metal solutions. *Ann. Phys.* **25**, 377–445 (1908).
64. M. W. Knight *et al.*, Aluminum for plasmonics. *ACS Nano* **8**, 834–840 (2014).
65. J. De Poorter *et al.*, Noninvasive MRI thermometry with the proton resonance frequency (PRF) method: In vivo results in human muscle. *Magn. Reson. Med.* **33**, 74–81 (1995).
66. J. De Poorter, Noninvasive MRI thermometry with the proton resonance frequency method: Study of susceptibility effects. *Magn. Reson. Med.* **34**, 359–367 (1995).
67. Y. Ishihara *et al.*, A precise and fast temperature mapping using water proton chemical shift. *Magn. Reson. Med.* **34**, 814–823 (1995).